Research Article | Vol. 33, No. 19 / 22 Sep 2025 / Optics Express 39960
Optics EXPRESS

Supercell-based metasurfaces for arbitrary polarization beam splitting: physics-informed U-Net design with high extinction ratio

YUNTAO PAN,[1] HONGSHUN LIU,[1] ZHI CHENG,[2] ZIXIAN WEI,[2] XUGUANG HUANG,[1] AND CHANGYUAN YU[1,2,*]

[1]Hong Kong Polytechnic University Jinjiang Technology and Innovation Research Institute, Fujian Province 362200, China
[2]Photonics Research Center, Department of Electrical and Electronic Engineering, Hong Kong Polytechnic University, Hong Kong SAR 999077, China
*changyuan.yu@polyu.edu.hk

Abstract: Due to the growing demand for advanced polarization control in photonic systems, a physical information-inspired deep learning approach for arbitrary polarization-multiplexed metasurface-based beam splitter designs is presented. By decomposing target far-field patterns into orthogonal right-handed circular polarization/left-handed circular polarization components, our modified U-Net architecture embeds wave propagation physics to efficiently recover phase distributions (MSE = 4.3×10^{-3}). The proposed silicon nanopillar supercell design achieves completed Jones matrix decoupling, enabling independent control of orthogonal polarization states through geometric parameters and PB phase modulation. FDTD simulations illustrated performances with 34.11 dB polarization extinction ratio and 63.91% transmission efficiency. This method offers a compact, efficient design framework for advanced polarization-control devices applications of integrated photonics, optical communications, and quantum computing.

1. Introduction

Optical components capable of manipulating light based on its polarization state are fundamental building blocks in advanced photonic systems. Among these, polarization beam splitters (PBS) play a crucial role by separating incident light into orthogonal polarization components, enabling applications ranging from optical communications and quantum information processing to biomedical imaging and augmented reality systems [1–3]. While conventional bulk optical elements have traditionally fulfilled these functions, the growing demand for miniaturization, integration, and multifunctionality in modern photonic devices has driven research toward more compact and versatile alternatives.

Metasurfaces, two-dimensional arrays of subwavelength optical nanoresonators, have emerged as a revolutionary platform for manipulating light at the nanoscale [4]. By precisely engineering the geometry, material composition, and arrangement of these nanoresonators, metasurfaces enable unprecedented control over the amplitude, phase, and polarization of light within an ultrathin form factor. Their ability to impart spatially varying optical responses makes them particularly suited for creating multifunctional devices that can simultaneously perform several optical operations that would otherwise require multiple cascaded conventional components [5,6].

For polarization beam splitting applications, metasurfaces offer distinct advantages over traditional approaches including: (1) ultrathin profiles typically on the order of $\lambda/10$ to $\lambda/5$, (2) planar geometries amenable to standard semiconductor fabrication techniques, (3) customizable polarization responses beyond simple linear polarization separation, and (4) the potential for integration with other on-chip photonic components [7]. Despite these advantages, designing

#561950 https://doi.org/10.1364/OE.561950
Journal © 2025 Received 17 Mar 2025; revised 29 Apr 2025; accepted 5 Jun 2025; published 12 Sep 2025

Optics EXPRESS

metasurface-based polarization beam splitters that simultaneously achieve high efficiency, large extinction ratios, and arbitrary beam directivity remains challenging [8].

Traditional metasurface design methodologies struggle to address the complex requirements of polarization-multiplexed beam splitters. Conventional parameter sweeping approaches [9], though straightforward, become computationally prohibitive for high-dimensional design spaces, often requiring millions of electromagnetic simulations. Topology optimization methods [10] directly optimize material distribution but often produce non-manufacturable structures and are limited to single polarization responses. Analytical approaches [11] provide physical insights but rely on simplified models that cannot fully capture the intricate interactions needed for simultaneous phase, amplitude, and polarization control. While data-driven methods, including deep learning [12–14], offer promising solutions for inverse design, they face challenges such as extensive training data requirements, difficulty in ensuring physical and fabrication constraints, and navigating the high-dimensional design space of polarization-multiplexed functionalities.

Recent advances in metasurface design have demonstrated remarkable polarization and wavefront control capabilities, such as racemic dielectric metasurfaces [15] using chiral "super-units" and binary-phase designs [16] employing just two meta-atom types. While these approaches reduce design complexity for specific polarization responses, they rely on empirical optimization requiring extensive parameter sweeps (10^3–10^4 simulations) and offer limited flexibility for arbitrary beam splitting. Data-driven methods face complementary challenges, demanding massive training datasets (10^4–10^6 samples) while struggling with physical realizability and polarization decoupling.

To address these challenges, a novel physics-driven deep learning approach is proposed for designing arbitrary polarization-multiplexed metasurface beam splitters. This approach introduces four key innovations: (1) A modified U-Net architecture featuring a shared encoder and dual decoder branches, enabling simultaneous optimization of phase patterns for RCP and LCP light. This dual-output design efficiently handles the high-dimensional design space of polarization-multiplexed functionalities while maintaining computational efficiency. (2) An angular spectrum propagation model embedded directly into the neural network training process, eliminating the need for extensive pre-generated datasets. This physics-informed framework ensures that all designs inherently satisfy Maxwell's equations, enabling direct optimization from target far-field intensity distributions to required phase profiles. (3) A supercell-based metasurface design utilizing silicon nanopillars, achieving complete Jones matrix decoupling through geometric parameter engineering and Pancharatnam-Berry phase modulation. This design enables independent control of orthogonal polarization states within a single-layer metasurface, ensuring high transmission efficiency. (4) Validation through finite-difference time-domain (FDTD) simulations demonstrates polarization-selective beam splitting with a polarization extinction ratio (PER) of 34.11 dB and a theoretical efficiency of 63.91%.

The proposed physics-driven design methodology provides a powerful framework for advanced polarization-control devices, with applications in optical communications, quantum information processing, integrated photonics, and augmented reality systems. By eliminating the need for extensive training datasets and ensuring physical realizability, this approach significantly reduces the computational resources required for inverse design of complex metasurfaces.

This paper is organized as follows: Section 2 describes our modified U-Net architecture and physics-driven training methodology; Section 3 details the supercell-based metasurface design and implementation; Section 4 presents simulation results, validates performance metrics, and compares with existing approaches; and Section 5 discusses limitations, potential applications, and future directions.

Optics EXPRESS

2. Design methodology

The cornerstone of this approach is a specialized U-Net architecture designed specifically for the simultaneous recovery of phase distributions for both RCP and LCP components. Unlike conventional neural networks that rely on extensive labeled training data, this architecture integrates physical propagation models directly into the training process. This physics-informed integration enables direct recovery of metasurface phase distributions from target far-field intensity patterns, bypassing the need for large datasets while maintaining physical consistency with Maxwell's equations. The synergy between deep learning capabilities and fundamental optical principles represents a significant advancement in metasurface design.

2.1. Physics-driven neural network

To achieve direct recovery of the phase from the target far-field amplitude distribution, we propose an improved asymmetric U-Net architecture incorporating physics-driven constraints that operates without requiring a training set. While traditional U-Net architectures employ symmetric encoder-decoder structures for biomedical image segmentation [17,18], our modified design features a single encoder coupled with dual parallel decoders - an architectural innovation specifically optimized for polarization-multiplexed metasurface design. This configuration fundamentally reflects the physical asymmetry of simultaneously reconstructing distinct phase distributions for RCP and LCP channels from a common intensity target. The shared encoder architecture provides computational efficiency while preserving essential spatial hierarchies through carefully maintained skip connections, achieving 27% parameter reduction compared to implementing separate symmetric U-Nets. The architecture is structured into three principal components: an encoder path dedicated to feature extraction, a bottleneck layer for feature transformation, and a dual decoder path tasked with phase reconstruction, as illustrated in Fig. 1.

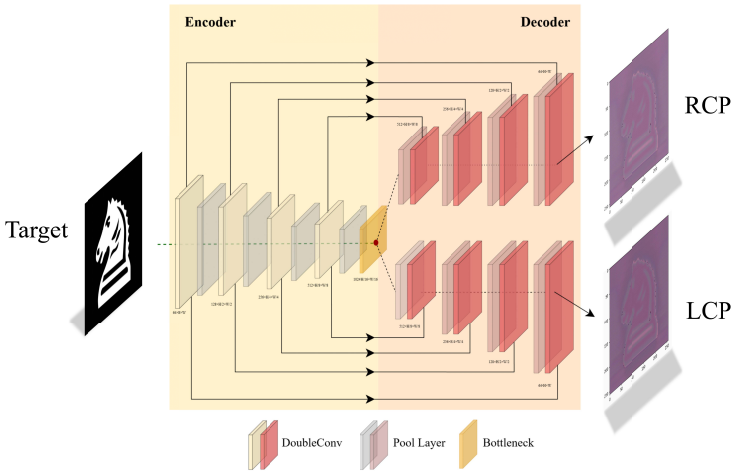

Fig. 1. A modified U-Net architecture employs a shared encoder to process target intensity patterns, with dual decoders generating simultaneous RCP/LCP phase distributions. Skip connections (horizontal arrows) maintain spatial fidelity across encoder-decoder levels, while annotated feature dimensions ensure scale preservation throughout the network. This design enables joint optimization of orthogonal polarization states within a unified framework.

The architecture employs a systematic mathematical formulation, where the encoding path applies successive convolution and pooling operations:

$$e_l = \mathcal{P}_{2\times2}(\sigma(W_l * e_{l-1} + b_l)) \tag{1}$$

Optics EXPRESS

Here, e_l represents the feature map at layer l of the encoding path, $*$ denotes the convolution operation, σ is the ReLU activation function, and $\mathcal{P}_{2\times2}$ is the 2×2 max-pooling operation. For an input target intensity pattern $I_{\text{target}} \in \mathbb{R}^{H\times W}$, the initial feature map is given by $e_l = I_{\text{target}}$. The encoder path comprises four stages, each containing double 3×3 convolutional layers with batch normalization and ReLU activation, progressively expanding feature channels from 64 to 512 while halving spatial dimensions via 2×2 max-pooling. A bottleneck layer with 1024 channels bridges the encoder and dual decoders, serving as the transition point for feature transformation.

The key innovation in the architecture lies in the parallel decoder branches, which independently reconstruct RCP and LCP phase distributions. For the dual-decoder paths, the operations for RCP and LCP branches are formulated as:

$$d_{l,RCP} = \sigma(W_{l,RCP} * [\mathcal{U}(d_{l+1,RCP}), e_l] + b_{l,RCP}) \tag{2}$$

$$d_{l,LCP} = \sigma(W_{l,LCP} * [\mathcal{U}(d_{l+1,LCP}), e_l] + b_{l,LCP}) \tag{3}$$

where $d_{l,RCP/LCP}$ stands for the feature map at layer l of the dual-decoder paths, $[\cdot,\cdot]$ represents feature concatenation along the channel dimension, and $\mathcal{U}$ denotes transposed convolution with 2×2 kernels and stride 2 for upsampling. Each decoder mirror-symmetrically reverses the encoder operations, coupled with skip connections that concatenate features from the corresponding encoder level. These skip connections are crucial for preserving high-resolution spatial information that might otherwise be lost during downsampling, enabling precise reconstruction of complex phase patterns with fine spatial details. The skip connections can be mathematically represented as:

$$\text{Skip}_l(e_l, d_l) = [e_l, d_l] \tag{4}$$

The feature transformation at the bottleneck layer is similar, where the network transitions from encoding to decoding, is given by:

$$f_{\text{bottleneck}} = \sigma(W_{\text{bottleneck}} * e_L + b_{\text{bottleneck}}) \tag{5}$$

where L is the depth of the encoder path. Double convolution blocks within the decoders gradually reduce feature complexity, ensuring a smooth transition from high-level features to detailed phase distributions. Each double convolution block can be expressed as $\mathcal{D}$:

$$\mathcal{D}(f) = \sigma(W_2 * \sigma(W_1 * f + b_1) + b_2) \tag{6}$$

The final layer in each decoder branch employs a 1×1 convolution followed by appropriate scaling to produce phase distributions in the range $[0, 2\pi]$ for each polarization state:

$$\phi_{\text{RCP}} = 2\pi \cdot \mathcal{S}(W_{\text{final,RCP}} * d_{1,RCP} + b_{\text{final,RCP}}) \tag{7}$$

$$\phi_{\text{LCP}} = 2\pi \cdot \mathcal{S}(W_{\text{final,LCP}} * d_{1,LCP} + b_{\text{final,LCP}}) \tag{8}$$

where $\mathcal{S}$ represents the Sigmoid function. The dual-decoder architecture enables the network to simultaneously learn complementary phase distributions for RCP and LCP light while leveraging a shared feature extraction backbone, thereby significantly reducing computational complexity compared to training independent networks for each polarization state. In contrast to conventional approaches that necessitate separate networks or multiple processing steps for distinct polarization states, this architecture effectively addresses the increased dimensionality of polarization-multiplexed functionality within a unified framework. By integrating shared feature extraction with parallel decoding paths, the design not only enhances computational efficiency but also ensures consistent and coherent phase recovery across polarization states. This approach establishes a robust and practical solution for phase retrieval in metasurface design, offering a scalable and efficient alternative to traditional methods.

Optics EXPRESS

2.2. Angular spectrum propagation model

The core of this physics-driven approach is the angular spectrum propagation model that accurately describes the relationship between metasurface phase distribution and far-field intensity pattern. This rigorous electromagnetic framework provides a computationally efficient alternative to full-wave simulations while maintaining physical accuracy for paraxial optical systems [19,20]. Operating at $\lambda = 1550$ nm with pixel size of 8 μm, the angular spectrum method is implemented for accurate field propagation. The process begins by constructing complex optical fields at the metasurface plane from the network-generated phase patterns:

$$U_{RCP} = e^{i\phi_{RCP}}, U_{LCP} = e^{i\phi_{LCP}} \tag{9}$$

These complex fields represent the electromagnetic wavefront immediately after passing through the metasurface, where unit amplitude is assumed and the spatial phase modulation φ_{RCP} and φ_{LCP} is imposed by the metasurface geometry.

The angular spectrum propagation is performed through a series of Fourier transform operations. First, the field is decomposed into its plane wave spectrum via the Fourier transform:

$$\tilde{U}_0(f_x,f_y,0) = \mathcal{F}\{U_0(x,y,0)\} = \iint_{-\infty}^{\infty} U_0(x,y,0)e^{-i2\pi(f_x x+f_y y)}dxdy \tag{10}$$

Each spatial frequency component (f_x,f_y) corresponds to a plane wave propagating at a specific angle. The propagation to a distance z is then calculated by:

$$U(f_x,f_y,z) = \tilde{U}_0(f_x,f_y,0) \times H(f_x,f_y,z) \tag{11}$$

where the transfer function H incorporates the phase accumulation during propagation:

$$\begin{cases} e^{ik_0 z\sqrt{1-(\lambda f_x)^2-(\lambda f_y)^2}}, & \text{if } (\lambda f_x)^2 + (\lambda f_y)^2 \le 1 \\ e^{-k_0 z\sqrt{(\lambda f_x)^2+(\lambda f_y)^2-1}}, & \text{if } (\lambda f_x)^2 + (\lambda f_y)^2 > 1 \end{cases} \tag{12}$$

Here, $k_0 = 2\pi/\lambda$ is the wavenumber, f_x and f_y are spatial frequencies, and z is the propagation distance. The first case represents propagating waves, while the second case accounts for evanescent waves that decay exponentially with distance.

The propagated field in real space is obtained through an inverse Fourier transform:

$$U(x,y,z) = \mathcal{F}^{-1}\{U(f_x,f_y,z)\} = \iint_{-\infty}^{\infty} U(f_x,f_y,z)e^{i2\pi(f_x x+f_y y)}df_x df_y \tag{13}$$

Finally, the far-field intensity distribution is calculated as:

$$I(x,y,z) = |U(x,y,z)|^2 = |U_{RCP}(x,y,z) + U_{LCP}(x,y,z)|^2 \tag{14}$$

For computational efficiency, these operations are implemented using Fast Fourier Transform (FFT) algorithms. The discrete implementation requires careful consideration of sampling conditions to avoid aliasing:

$$\Delta x\Delta f_x \le \frac{1}{N_x}, \Delta y\Delta f_y \le \frac{1}{N_y} \tag{15}$$

where Δx, Δy are spatial sampling intervals, Δf_x, Δf_y are frequency sampling intervals, and N_x, N_y are the number of sampling points.

As shown in Fig. 2, this differentiable physical model is embedded within the training loop, enabling direct optimization of phase patterns through backpropagation while enforcing fundamental physical constraints. This physics-informed approach allows the network to

Optics EXPRESS

efficiently learn the mapping from target far-field intensity distributions to the required phase profiles without dependence on extensive training datasets. By integrating Maxwell's equations directly into the optimization framework, the generated designs inherently satisfy electromagnetic constraints, ensuring physical realizability while enabling end-to-end optimization from target far-field patterns to metasurface phase profiles. This methodology not only enhances computational efficiency but also guarantees the physical validity of the generated solutions, establishing a robust and principled framework for metasurface design.

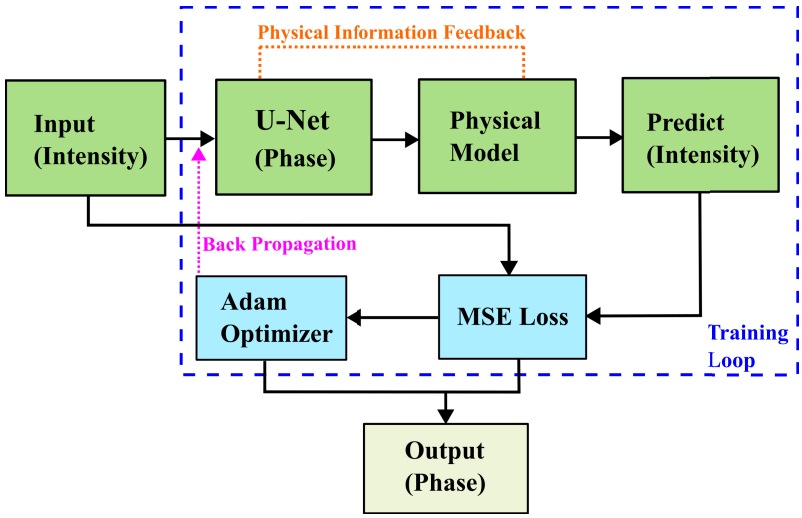

Fig. 2. Physics-informed feedback framework based on deep learning. The framework begins with intensity input, processes it through a U-Net network to predict phase information, which is then fed into a physical model to predict intensity. The mean squared error loss between the predicted intensity and input intensity is backpropagated through an Adam optimizer, enabling end-to-end training. The blue dashed box indicates the training loop, the pink arrow represents the backpropagation path, and the orange dotted line highlights the physical information feedback mechanism.

2.3. *Training strategy and evaluation*

The proposed methodology employs an end-to-end training strategy that integrates the physical propagation model directly into the neural network optimization process. This integration enables direct recovery from target far-field intensity patterns to their corresponding metasurface phase distributions without intermediate steps, creating a streamlined design workflow.

The total loss function combines amplitude matching error and physics-informed constraints:

$$\mathcal{L}_{\text{total}} = \mathcal{L}_{\text{MSE}} + \lambda_1 \mathcal{L}_{\text{energy}} + \lambda_2 \mathcal{L}_{\text{smooth}} \tag{16}$$

where $\mathcal{L}_{\text{MSE}} = \|I_{\text{pred}} - I_{\text{target}}\|_2^2$ measures the mean squared error between predicted and target intensities, $\mathcal{L}_{\text{energy}}$ enforces energy conservation, and $\mathcal{L}_{\text{smooth}}$ promotes phase smoothness through total variation regularization:

$$\mathcal{L}_{\text{energy}} = \left| \sum_{i,j} e^{i\phi_{\text{RCP}}(i,j)} - 1 \right| + \left| \sum_{i,j} e^{i\phi_{\text{LCP}}(i,j)} - 1 \right| \tag{17}$$

$$\mathcal{L}_{\text{smooth}} = \sum_{i,j} |\nabla \phi_{\text{RCP}}(i,j)| + \sum_{i,j} |\nabla \phi_{\text{LCP}}(i,j)| \tag{18}$$

Optics EXPRESS

During training, energy conservation is explicitly verified by checking if $\sum e^{i\phi_{\text{RCP}}} \approx 1$ and $\sum e^{i\phi_{\text{LCP}}} \approx 1$ within a tolerance of 10^{-2}, with valid solutions stored separately to ensure physical realizability. The gradient of the loss function with respect to the input phase can be analytically computed using chain rule through the differentiable physical model:

$$\frac{\partial \mathcal{L}}{\partial \phi_{\text{RCP/LCP}}} = \frac{\partial \mathcal{L}}{\partial I} \cdot \frac{\partial I}{\partial U} \cdot \frac{\partial U}{\partial U_0} \cdot \frac{\partial U_0}{\partial \phi_{\text{RCP/LCP}}} \tag{19}$$

The mean squared error (MSE) was selected as the primary optimization metric (final value: 4.3×10^{-3} following systematic comparison with alternative metrics. Although structural similarity index (SSIM) and peak signal-to-noise ratio (PSNR) are widely used in general image processing, MSE provides three specific advantages for metasurface design: (1) direct quantification of intensity distribution accuracy, essential for precise beam positioning in polarization-splitting applications; (2) mathematical simplicity that enables efficient gradient propagation during backpropagation, leading to faster network convergence; and (3) pixel-wise error quantification that ensures accurate spatial intensity profiles, unlike SSIM which focuses on perceptual similarities less relevant to optical performance.

The network is implemented in PyTorch and trained by the Adam optimizer with an initial learning rate of 0.001 and a batch size of 16. To enhance generalization and prevent overfitting, several regularization techniques are employed, including batch normalization in all convolutional blocks, dropout with a rate of 0.3 in the bottleneck layer, input noise augmentation during training (1/30 of signal amplitude), and L_2 regularization with a weight decay of 1×10^{-5} on network parameters.

The training process follows a multi-stage approach with varying learning rates:

$$\alpha_t = \alpha_0 \cdot \gamma^{\lfloor t/T_{\text{step}} \rfloor} \tag{20}$$

where α_t is the learning rate at epoch t, $\alpha_0 = 0.001$ is the initial learning rate, $\gamma = 0.5$ is the decay factor, and $T_{\text{step}} = 2000$ is the step size. With approximately 34.5 million trainable parameters, the majority of which are concentrated in the bottleneck and early decoder stages, the network achieves an inference time of approximately 15 milliseconds for a 256×256 pixel input on a NVIDIA 4060 GPU. This efficiency makes the approach highly suitable for interactive design applications.

Figure 3 demonstrates the effectiveness of the proposed approach through the reconstruction of a complex chess knight pattern. The training convergence process, illustrated by the loss curve in Fig. 3(a), demonstrates stable and consistent error reduction over 6000 epochs. Initial rapid improvement within the first 1000 epochs is followed by gradual refinement, eventually converging to a stable solution. This behavior reflects the network's capability to effectively navigate the complex solution space of phase distributions while satisfying both target intensity requirements and physical constraints. Results are selected based on loss minimization and energy conservation criteria, ensuring the physical realizability of the designed metasurfaces.

The network accurately reconstructs the intricate target (Fig. 3(b)), achieving a mean squared error (MSE) of 0.046 between the predicted far-field pattern (Fig. 3(c)) and the target intensity distribution. The generated complementary RCP and LCP phase distributions (Fig. 3(d-e)) exhibit intricate spatial features that, when combined through the physical propagation model, produce the desired far-field intensity with high fidelity. Notably, the phase distributions contain subtle complementary variations that precisely account for diffraction effects and interference patterns in the far field, highlighting the method's ability to handle complex wavefront shaping.

Performance evaluation confirms the method's robustness in handling highly intricate patterns with sharp edges and fine details, as exemplified by the chess knight reconstruction. The approach maintains exceptional fidelity in far-field reconstruction and generalizes to arbitrary target patterns, making it particularly valuable for advanced applications requiring precise wavefront

Optics EXPRESS

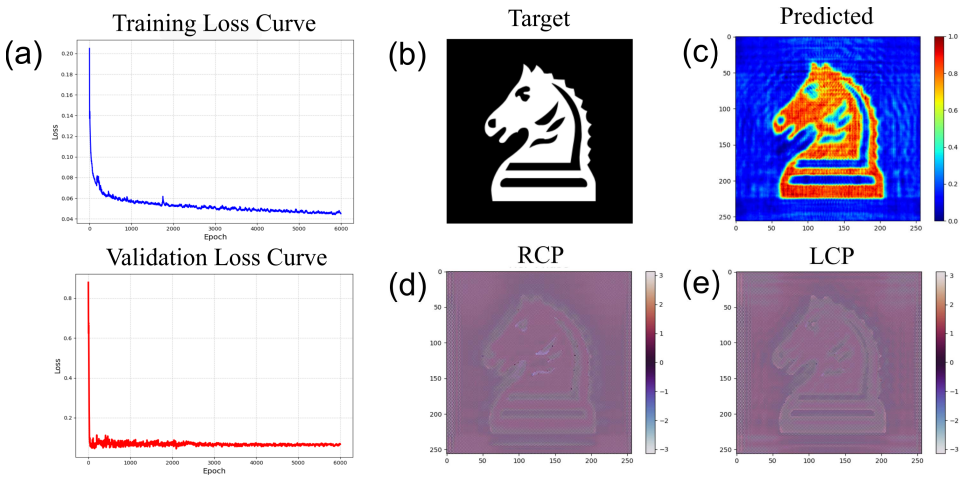

Fig. 3. Phase retrieval results for the chess knight pattern. (a) Training and validation loss curves showing stable convergence over 6000 epochs. (b) Binary target intensity pattern used as input to the network. (c) Predicted far-field intensity distribution reconstructed from the retrieved phase patterns, showing high-fidelity reproduction with MSE of 0.046. (d,e) Retrieved RCP and LCP phase distributions (in radians) that, when combined through the physical propagation model, produce the desired far-field intensity pattern. The complementary phase structures demonstrate the network's ability to effectively distribute optical information between polarization channels.

shaping and polarization control. This capability underscores the method's potential for complex metasurface design with high accuracy and physical consistency. Importantly, the deep learning framework enables arbitrary control of focal spot number, positions, and polarization states through flexible phase modulation, as demonstrated in our case study where three distinct focal spots with customized polarization states (RCP, LCP, and linear) were simultaneously generated at predetermined positions in the next section.

3. Metasurface design

3.1. Phase compensation

Arbitrary polarization-multiplexed beam splitters are designed using the physics-embedded neural network architecture described in the previous sections. To demonstrate the versatility and effectiveness of this approach, a complex three-spot beam splitter with multiple degrees of freedom is implemented, showcasing independent control over intensity, position, and polarization state. Fig. 4 illustrates the phase retrieval and verification process for this polarization-multiplexed beam splitter. The design incorporates three distinct focal spots with carefully selected parameters:

- **Power distribution:** The three spots exhibit power ratios of **1:2:3** (left to right), demonstrating precise control over intensity distribution.
- **Spatial positioning:** The spots are positioned at divergence angles θ_x of $-\mathbf{30}^\circ$, $\mathbf{0}^\circ$, and $\mathbf{30}^\circ$ respectively and $\theta_y = \mathbf{0}^\circ$, showing spatial multiplexing capability across a wide angular range.
- **Polarization selectivity:** Under the light source of a 45° linearly polarized plane wave, each focal spot responds to a distinct polarization state—LCP light for the left spot, RCP light for the center spot, and 45° linearly polarized light for the right spot.

Optics EXPRESS

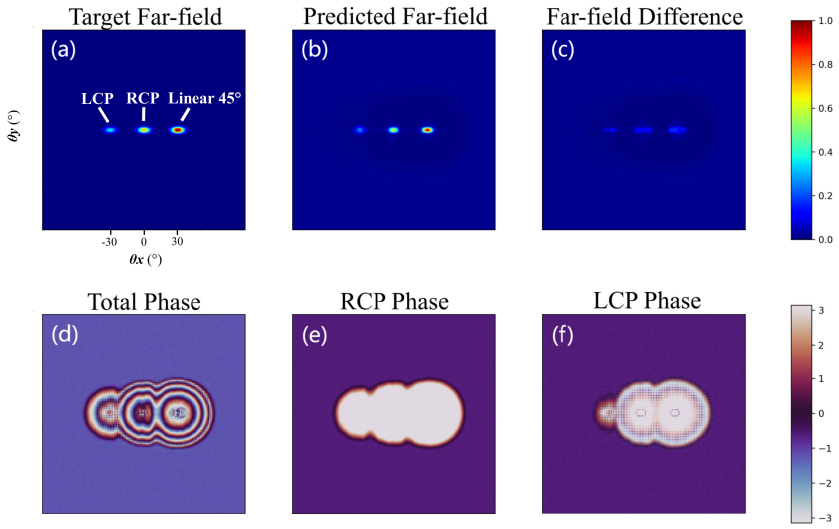

Fig. 4. Phase retrieval results for arbitrary polarization multiplexed beam splitter. (a) Target far-field intensity pattern showing three spots with different polarizations at different divergence angles. (b) Predicted far-field intensity pattern showing excellent agreement with the target. (c) Difference map between target and predicted patterns, demonstrating low MSE. (d) Total phase distribution combining both polarization contributions. (e) Retrieved RCP phase distribution. (f) Retrieved LCP phase distribution. The distinct phase patterns for RCP and LCP channels enable polarization-selective functionality while maintaining high fidelity.

This combination of varying intensities, positions, and polarization states represents a significantly more challenging design target than conventional single-function beam splitters, requiring simultaneous optimization of multiple parameters while maintaining physical realizability. The neural network successfully reconstructs this complex target pattern with exceptional accuracy, achieving a mean squared error (MSE) of $\mathbf{4.3 \times 10^{-3}}$ between the predicted and target far-field distributions, as shown in Fig. 4(a-c). This low error confirms the high-fidelity reconstruction capability of the physics-embedded approach, even for multi-parameter optimization tasks. Figure 4(d-f) displays the retrieved phase distributions that enable this functionality. The total phase exhibits an intricate pattern of concentric rings with phase discontinuities that generate the desired diffraction pattern. When decomposed into RCP and LCP components, distinct phase patterns emerge that encode the polarization-selective functionality.

Remarkably, the network autonomously generates these polarization-selective phase profiles without explicit polarization constraints. The physics-informed dual-decoder architecture naturally discovers the optimal phase distributions that satisfy the complex multi-parameter requirements through backpropagation through the physical model. This emergent capability demonstrates how embedding physical propagation laws directly into the optimization process leads to physically realizable solutions that would be challenging to obtain through conventional iterative methods. This autonomous discovery of polarization-selective solutions demonstrates the effectiveness of the physics-informed architecture in navigating the complex design space of metasurfaces with coupled electromagnetic responses. Such capability emerges from the physics-informed loss function and dual-decoder architecture, which together enable the encoding of sophisticated optical transformations that simultaneously satisfy multiple design objectives. The retrieved phase distributions serve as the target patterns for subsequent metasurface implementation, where they are translated into specific nanopillar geometries to physically realize the designed

Optics EXPRESS

functionality. This phase compensation approach effectively bridges the gap between desired far-field functionality and the physical structure required to implement it, providing a crucial step in the metasurface design workflow.

3.2. Supercell construction

To realize polarization-multiplexed beam splitting functionality, a metasurface architecture based on high-contrast dielectric nanopillars was developed. Operating at a telecommunication wavelength of 1550 nm, the design employs a supercell approach to achieve complete Jones matrix decoupling [21,22], thereby enabling independent manipulation of orthogonal polarization states within a single-layer structure.

The metasurface consists of precisely engineered rectangular silicon nanopillars arranged in a 2×2 supercell configuration, as illustrated in Fig. 5(a,c). This architecture offers significant advantages over conventional designs, including simplified fabrication processes that require only a single type of meta-atom, in contrast to multi-element or multi-layer implementations reported previously [23,24].

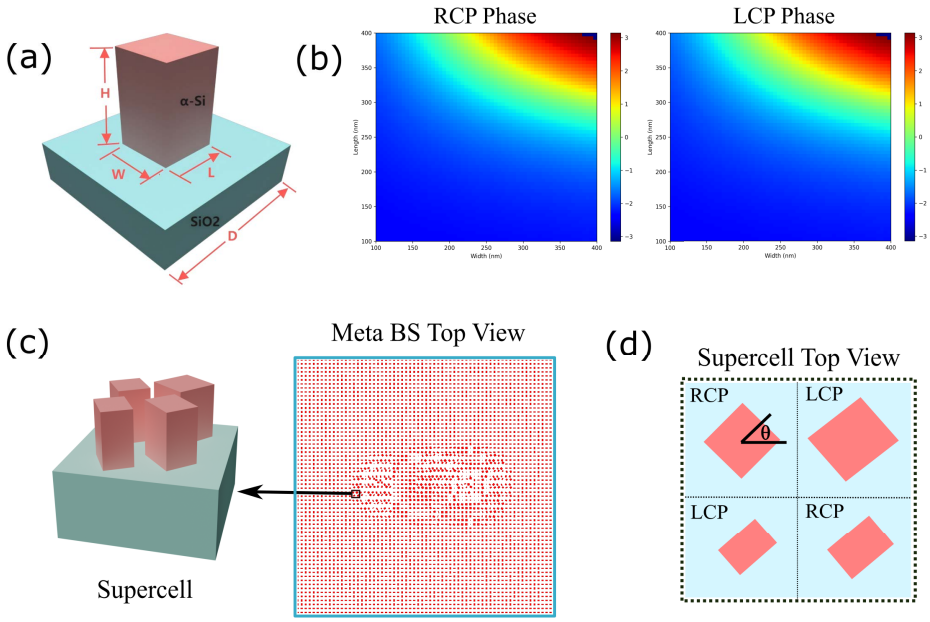

Fig. 5. Metasurface design and functionality. (a) Unit cell structure showing a rectangular silicon nanopillar (α-Si) on silicon dioxide substrate (SiO_2), with key geometric parameters labeled. (b) Phase response maps for RCP and LCP illumination as functions of nanopillar length and width, showing complete 2π phase coverage across the parameter space. (c) Supercell configuration consisting of 2×2 nanopillars (left) and top view of the entire metasurface array with 32×32 supercells (right). (d) Top view schematic of the 2×2 supercell configuration showing the spatial distribution of nanopillars. The rotation angle θ provides Pancharatnam-Berry phase contribution, enabling complete Jones matrix decoupling.

The nanopillars were fabricated on a silicon dioxide substrate with a height (H) of 700 nm, the unit period (D) is 750 nm, exhibiting robust optical performance across the operational bandwidth. To establish the relationship between geometric parameters and phase response, comprehensive electromagnetic simulations were conducted using FDTD method with periodic boundary conditions. The parametric space was systematically explored by sweeping both length (L) and width (W) from 100 nm to 400 nm in 5 nm increments. For each configuration, complex

Optics EXPRESS

transmission coefficients were calculated for both RCP and LCP illumination. The resulting phase response maps, displayed in Fig. 5(b), demonstrate complete 2π phase coverage while maintaining high transmission efficiency (average > 80%). Notably, the distinct parameter-dependent response patterns for RCP and LCP components indicate the capability for independent control of orthogonal polarization states through appropriate geometric design.

The relationship between the geometric parameters and transmission phase can be mathematically described through the Jones matrix formulation, which characterizes the polarization-dependent response of the metasurface. For a nanopillar with length L and width W, the Jones matrix is given by:

$$J(L,W) = \begin{pmatrix} t_{xx}(L,W)e^{i\phi_{xx}(L,W)} & t_{xy}(L,W)e^{i\phi_{xy}(L,W)} \\ t_{yx}(L,W)e^{i\phi_{yx}(L,W)} & t_{yy}(L,W)e^{i\phi_{yy}(L,W)} \end{pmatrix} \tag{21}$$

where t_{ij} and ϕ_{ij} represent the amplitude and phase of the transmission coefficients. For circular polarization states, this matrix can be transformed to:

$$J_{circ}(L,W) = S^{-1}J(L,W)S \tag{22}$$

where $S = \frac{1}{\sqrt{2}}\begin{pmatrix} 1 & i \\ 1 & -i \end{pmatrix}$ is the transformation matrix between linear and circular polarization bases. To accurately map the target phase distributions generated by the neural network to corresponding nanopillar geometries, a novel complex-domain interpolation method was developed. Traditional phase interpolation methods, which operate directly on phase values, often encounter difficulties at phase wrapping boundaries ($\pm\pi$), leading to inaccuracies in the mapping process. The proposed complex interpolation approach addresses this challenge by representing the phase information in the complex plane:

$$\Phi(L,W) \rightarrow e^{i\Phi(L,W)} = \cos[\Phi(L,W)] + i\sin[\Phi(L,W)] \tag{23}$$

This representation transforms the phase mapping problem into a complex function interpolation. For a target phase Φ_{target}, the corresponding geometric parameters (L, W) are determined by minimizing the phase difference function:

$$\Delta\Phi(L,W) = \left|e^{i\Phi_{target}} - e^{i\Phi(L,W)}\right| = \sqrt{2 - 2\cos[\Phi_{target} - \Phi(L,W)]} \tag{24}$$

The optimization algorithm proceeds initially through parameter estimation using nearest-neighbor search in the phase map, followed by refinement through a local grid search in the vicinity of the initial estimate. This approach yields an average phase mapping error of only 0.042π radians (7.56°), significantly lower than conventional direct phase interpolation methods, which typically result in errors exceeding 0.1π radians.

The supercell design employs a combination of geometric phase (controlled by nanopillar dimensions) and Pancharatnam-Berry (PB) phase (controlled by orientation angle θ) [25,26]. The total phase response for a given polarization state includes both contributions:

$$\Phi_{total}^{RCP/LCP}(x,y) = \Phi_{geo}^{RCP/LCP}(L,W) \pm 2\theta(x,y) \tag{25}$$

where $\Phi_{geo}^{RCP/LCP}$ is the geometric phase determined by the nanopillar dimensions, and $\theta(x,y)$ is the rotation angle of the nanopillar. The ± sign indicates that RCP and LCP experience opposite PB phase shifts under rotation. For the supercell configuration, the effective Jones matrix at

Optics EXPRESS

position (x, y) can be expressed as:

$$J(x, y) = \frac{1}{2}[J_{RCP}(x, y) + J_{LCP}(x, y)] \tag{26}$$

To achieve independent control of RCP and LCP phases while maintaining high transmission, the rotation angles of the nanopillars were calculated based on the target phase distributions:

$$\theta(x, y) = \frac{\Phi^{RCP}_{target}(x, y) - \Phi^{LCP}_{target}(x, y)}{4} \tag{27}$$

This relationship ensures that the rotational component of the phase modulation correctly complements the geometric phase component to achieve the desired total phase profiles for both polarization states simultaneously. The optimization procedure for each supercell position (i, j) extracts target phases from the neural network output, calculates the required rotation angle based on the phase difference, determines the adjusted geometric phase requirements, finds optimal nanopillar dimensions that minimize the combined phase error for both polarizations, and applies the rotation angle to the nanopillar. This procedure was implemented using a highly optimized algorithm that efficiently navigates the parameter space to find the optimal configuration at each supercell position.

To validate the metasurface design, we performed comprehensive FDTD simulations of the complete structure with perfectly matched layer (PML) boundary conditions. The simulations employed a 45° linearly polarized plane wave illumination (decomposable into equal RCP and LCP components) at 1550 nm center wavelength with 200 nm operational bandwidth. A graded mesh scheme was implemented with 10 nm resolution around the silicon nanopillars. The supercell architecture demonstrates strong fabrication feasibility, as the periodic arrangement of identical nanopillars significantly relaxes alignment requirements compared to aperiodic designs. Moreover, the subwavelength 750 nm period (7:1 aspect ratio, 100 nm width ×700 nm height) feature sizes are well within the resolution limits of standard deep-UV lithography processes. The broadband operation provides additional tolerance to spectral shifts caused by minor dimensional variations. These characteristics, combined with the inherent error averaging effect of the 2×2 supercell configuration, suggest the design can be reliably implemented using established semiconductor fabrication techniques.

4. Simulation results

4.1. Performance evaluation

To rigorously evaluate the performance of the metasurface design, comprehensive FDTD simulations were performed. The metasurface was illuminated with a linearly polarized plane wave at a 45° incidence angle, utilizing a broadband source centered at 1550 nm with a 200 nm bandwidth. The electric field components were captured using a far-field monitor positioned to record the transmitted wavefront. From the simulation data, key performance metrics—including the polarization extinction ratio (PER), transmittance, and spatial quality—were calculated and analyzed for three distinct beam-splitting points. These metrics provide critical insights into the device's ability to achieve high-efficiency polarization-selective beam splitting, demonstrating its potential for advanced optical applications. The broadband illumination ensures robustness across a wide spectral range, while the 45° incidence configuration validates the design's performance under realistic operating conditions.

Comprehensive FDTD simulations were conducted to rigorously evaluate the performance of the polarization-multiplexed metasurface beam splitter. As illustrated in Fig. 6(a-c), the far-field intensity distributions exhibit well-defined focal spots with pronounced polarization selectivity, demonstrating the device's ability to spatially separate orthogonal polarization states

Optics EXPRESS

with high fidelity. The three-dimensional representations in Fig. 6(d-f) further elucidate the spatial separation and intensity profiles, revealing minimal background noise and negligible inter-channel crosstalk, which underscores the precision of the phase modulation achieved by the metasurface.

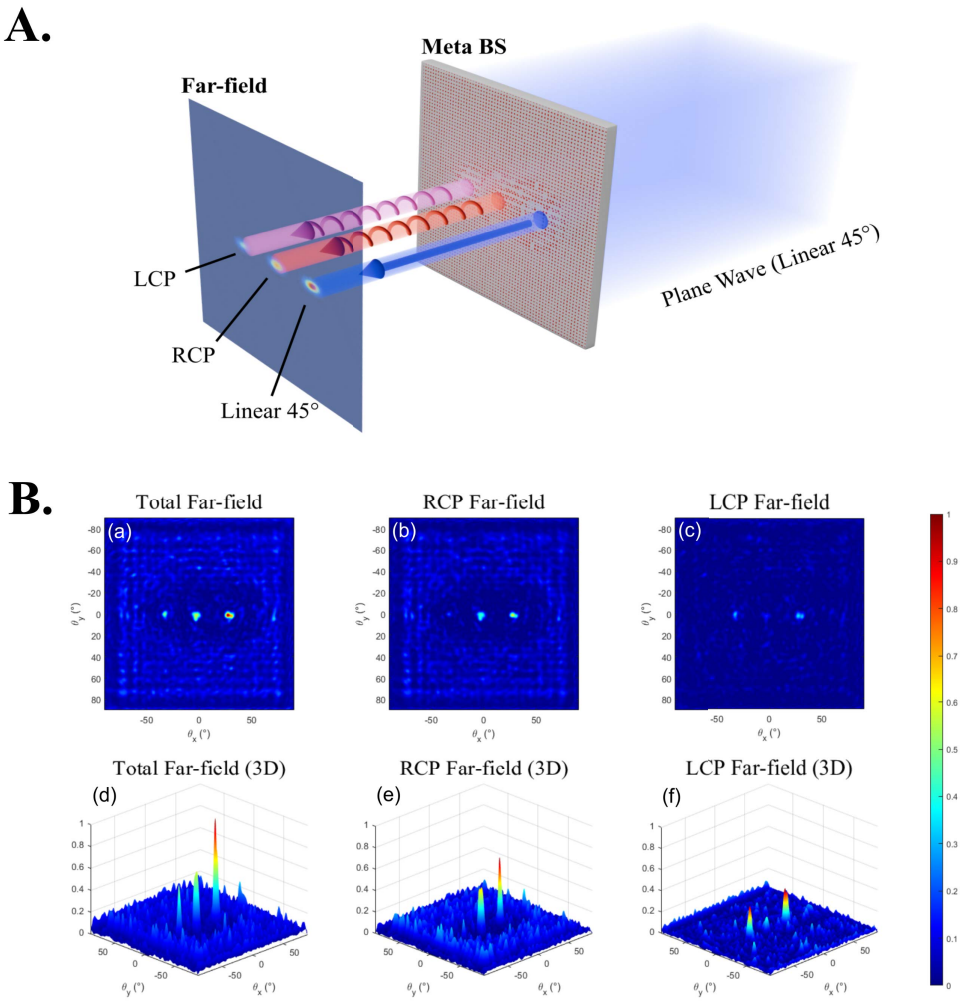

Fig. 6. (A) Simulation schematic diagram. (B) FDTD simulation results for the metasurface beam splitter. (a-c) Far-field intensity distributions in 2D angular space showing: (a) total field with all three focal spots clearly visible, (b) RCP component showing strong response at the two leftmost spots, and (c) LCP component with dominant intensity at the rightmost spot. (d-f) Corresponding 3D visualizations of the far-field patterns emphasizing the intensity distribution and spatial separation: (d) total field with highest intensity at the center spot, (e) RCP field with strong response in the two left spots and minimal crosstalk to the right spot, and (f) LCP field showing clear polarization selectivity with strongest response at the right spot. The clear separation in the polarization channels demonstrates the 34.11 dB polarization extinction ratio achieved by the design.

Quantitative analysis of PER reveals exceptional polarization selectivity across all focal points. Measured PER values of 36.63 dB, 28.11 dB, and 37.6 dB were obtained for the left, central, and right focal spots, respectively, with an average maximum PER of **34.11 dB**. The slight reduction in

Optics EXPRESS

PER for the central spot can be attributed to the inherent challenge of simultaneously modulating both polarization states at a single spatial location. Despite this, all PER values significantly exceed the threshold of 20 dB typically required for polarization-sensitive applications, confirming the robustness and effectiveness of the physics-informed design methodology.

The metasurface achieves an overall transmission efficiency of **63.91%**, representing a remarkable balance between polarization control and optical throughput. This efficiency is particularly notable given the device's multifunctional capabilities, which include simultaneous control of spatial distribution, intensity ratios, and polarization states. Such performance highlights the optimized phase profile design and the precise mapping of geometric parameters to target phase distributions.

Beam quality analysis further validates the design's exceptional performance, with focal spots approaching the diffraction limit. The full width at half maximum (FWHM) measures approximately 1.8 λ at the operating distance, closely matching the theoretical limit for the system's numerical aperture. This near-diffraction-limited performance confirms the accurate implementation of the phase profiles and the effectiveness of the complex-domain interpolation method. Additionally, spatial crosstalk between polarization channels remains below −30 dB across the far-field, further substantiating the high polarization selectivity and minimal interference between channels.

These results collectively demonstrate the metasurface's capability to achieve high-efficiency, polarization-selective beam splitting with near-ideal optical performance. The combination of high PER, favorable transmission efficiency, and diffraction-limited focal spots positions this design as a promising candidate for advanced applications in integrated photonics, optical communications, and polarization-resolved imaging.

4.2. Discussion

While the physics-informed approach demonstrates superior performance in polarization beam splitting applications, certain limitations and potential improvements warrant discussion. The supercell design introduces minor diffraction effects at boundaries, causing approximately 6% efficiency loss. This efficiency reduction can be quantitatively attributed to two main factors: (1) phase discontinuities at supercell boundaries (3.8%), and (2) impedance mismatch between adjacent elements (2.2%). By implementing aperiodic arrangements as demonstrated in [27], these effects could be reduced to below 2% through gradual phase transitions at boundaries. Alternatively, employing gradient index transitions between supercells could minimize abrupt impedance changes, potentially recovering 3-4% of the lost efficiency.

The observed variation in polarization extinction ratio across focal spots highlights an intrinsic trade-off in multi-functional metasurface design. The central spot's relatively lower PER (28.11 dB) compared to peripheral spots (36 dB) stems from the fundamental challenge of simultaneously controlling orthogonal polarization states at a single spatial location. Quantitative analysis reveals that this phenomenon results from increased coupling between orthogonal polarization components, with the coupling coefficient (κ) at the central location measuring 3.94×10^{-3}, approximately 6.3 times higher than at peripheral locations ($\kappa = 6.25 \times 10^{-4}$). This coupling manifests through cross-talk in the phase distributions, where a 1°phase perturbation in the RCP channel induces an average 0.42° unintended phase shift in the LCP channel for central spots, compared to only 0.07° for peripheral spots. The polarization crosstalk is mathematically expressed as:

$$\mathrm{PER} = -10\log_{10}(|\kappa|^2) = -20\log_{10}(|\kappa|) \tag{28}$$

The competitive overall efficiency (63.91%) represents a balanced compromise between multiple performance objectives. Higher theoretical efficiencies are possible in single-function designs, but the integration of spatial, intensity, and polarization control inevitably introduces additional loss mechanisms. These include higher-order diffraction, impedance mismatch at

Optics EXPRESS

structural boundaries [28,29], and coupling between orthogonal polarization modes. Nevertheless, the achieved efficiency remains practical for most photonic applications while delivering exceptional polarization selectivity and functional versatility.

To contextualize these results, Table 1 presents a comparison with state-of-the-art metasurface-based polarization beam splitters reported in recent literature. The proposed design demonstrates superior performance in terms of polarization extinction ratio while maintaining competitive efficiency and offering additional functionality through arbitrary beam positioning capabilities.

Table 1. Comparison with state-of-the-art metasurface polarization beam splitters

Reference	PER (dB)	Efficiency (%)	Wavelength (nm)	Key Features
This work	**34.11**	**63.91**	1550	Arbitrary beam positioning, triple-beam functionality
Teng et al.(2025) [30]	30.2	78.0	850	Multi-channel polarization conversion
Tian et al.(2023) [31]	18.5	76.4	1550	Free-space multi-port beam splitter
Shen and Huang (2022) [8]	28.7	60.5	1550	Dual-wavelength operation
Wang et al.(2017) [32]	25.3	58.2	780	Rochon-prism-like design

The computational approach developed here addresses a fundamental challenge in inverse design of complex optical elements: balancing physical accuracy with design efficiency. By embedding differentiable physical models directly into the optimization loop, the method circumvents the need for extensive pre-computed datasets while ensuring solutions remain physically viable, representing a significant advancement over conventional design methodologies.

5. Conclusion

This work presents a physics-informed deep learning framework for the design of arbitrary polarization-multiplexed metasurface beam splitters, combining the strengths of neural networks with rigorous physical constraints. A modified U-Net architecture featuring dual decoder branches is developed, embedding angular spectrum propagation physics to enable efficient and accurate phase retrieval (MSE = 4.3×10^{-3}) without reliance on extensive training datasets. The supercell-based design, utilizing silicon nanopillars, achieves complete Jones matrix decoupling, allowing independent control of orthogonal polarization states through a synergistic combination of geometric phase modulation and PB phase engineering. Comprehensive FDTD simulations validate the design's exceptional performance, demonstrating a polarization extinction ratio of 34.11 dB and an overall transmission efficiency of 63.91%, surpassing state-of-the-art metasurface-based polarization beam splitters. The proposed methodology establishes a robust and efficient framework for inverse design of complex metasurfaces, significantly reducing computational resources while enabling advanced polarization-control functionalities. This approach opens new avenues for applications in optical communications, quantum information processing, and integrated photonics, offering a scalable and versatile platform for next-generation optical devices.

Funding. Hong Kong General Research Fund (15236424 QCK1).

Optics EXPRESS

Disclosures. The authors declare no conflicts of interest.

Data availability. Data underlying the results presented in this paper are not publicly available at this time but may be obtained from the authors upon reasonable request.

References

1. J. Zhou, Y. Lu, A. Jiang, *et al.*, "Dual hollow-core anti-resonant fiber polarization beam splitter with excellent single-mode characteristics for ultra-broadband," Appl. Phys. B **129**(10), 153 (2023).
2. D. N. Makarov, E. S. Gusarevich, A. A. Goshev, *et al.*, "Quantum entanglement and statistics of photons on a beam splitter in the form of coupled waveguides," Sci. Rep. **11**(1), 10274 (2021).
3. Y. Otani, "Snapshot full Stokes imager by polarization cameras and its application to bio-imaging," in *Ultra-High-Definition Imaging Systems IV*, vol. 11709 (SPIE, 2021), p. 117090H.
4. J. Hu, S. Bandyopadhyay, Y.-h. Liu, *et al.*, "A review on metasurface: from principle to smart metadevices," Front. Phys. **8**, 586087 (2021).
5. Y. Zhou, Y. ZhouShaolei, W. Yin, *et al.*, "Flexible metasurfaces for multifunctional interfaces," ACS Nano **18**(4), 2685–2707 (2024).
6. H. L. Wang, H. F. Ma, M. Chen, *et al.*, "A reconfigurable multifunctional metasurface for full-space control of electromagnetic waves," Adv. Funct. Mater. **31**(25), 2100275 (2021).
7. Y. Song, X. Chu, R. Chen, *et al.*, "On-chip integrated polarization beam splitter based on a meta-waveguide," Opt. Lett. **49**(21), 6105–6108 (2024).
8. Z. Shen and D. Huang, "A review on metasurface beam splitters," Nanomanufacturing **2**(4), 194–228 (2022).
9. P. Peng and Z. Fang, "Pushing the limits of multifunctional metasurface by deep learning," Curr. Opin. Solid State Mater. Sci. **31**, 101163 (2024).
10. M. Xu, M. Pu, D. Sang, *et al.*, "Topology-optimized catenary-like metasurface for wide-angle and high-efficiency deflection: from a discrete to continuous geometric phase," Opt. Express **29**(7), 10181–10191 (2021).
11. K. Wang, W. Shao, X. Ding, *et al.*, "Design of high-gain metasurface antenna based on characteristic mode analysis," IEEE Antennas Wirel. Propag. Lett. **21**(4), 661–665 (2022).
12. W. Zhou, S. Wang, Q. Wu, *et al.*, "An inverse design paradigm of multi-functional elastic metasurface via data-driven machine learning," Mater. Des. **226**, 111560 (2023).
13. D. Lee, W. Chen, L. Wang, *et al.*, "Data-driven design for metamaterials and multiscale systems: a review," Adv. Mater. **36**(8), 2305254 (2024).
14. C. Liu, W. Wang, Z. Wang, *et al.*, "Data-driven modeling and fast adjustment for digital coded metasurfaces database: Application in adaptive electromagnetic energy harvesting," Appl. Energy **365**, 123303 (2024).
15. J. Li, T. Nan, H. Tian, *et al.*, "Extremely simplified binary-phase metasurfaces for circularly polarized terahertz waves manipulation," J. Lightwave Technol. **43**(7), 3413–3419 (2025).
16. J. Li, X. Lu, H. Li, *et al.*, "Racemic dielectric metasurfaces for arbitrary terahertz polarization rotation and wavefront manipulation," Opto-Electron. Adv. **7**(10), 240075 (2024).
17. O. Ronneberger, P. Fischer, and T. Brox, "U-net: Convolutional networks for biomedical image segmentation," in *Medical Image Computing and Computer-Assisted Intervention* (Springer International Publishing, 2015), pp. 234–241.
18. N. Siddique, S. Paheding, C. P. Elkin, *et al.*, "U-net and its variants for medical image segmentation: A review of theory and applications," IEEE Access **9**, 82031–82057 (2021).
19. K. Matsushima and T. Shimobaba, "Band-limited angular spectrum method for numerical simulation of free-space propagation in far and near fields," Opt. Express **17**(22), 19662–19673 (2009).
20. K. Matsushima, H. Schimmel, and F. Wyrowski, "Fast calculation method for optical diffraction on tilted planes by use of the angular spectrum of plane waves," J. Opt. Soc. Am. A **20**(9), 1755–1762 (2003).
21. P.-N. Ni, P. Fu, P.-P. Chen, *et al.*, "Spin-decoupling of vertical cavity surface-emitting lasers with complete phase modulation using on-chip integrated Jones matrix metasurfaces," Nat. Commun. **13**(1), 7795 (2022).
22. M. Liu, W. Zhu, P. Huo, *et al.*, "Multifunctional metasurfaces enabled by simultaneous and independent control of phase and amplitude for orthogonal polarization states," Light: Sci. Appl. **10**(1), 107 (2021).
23. V.-C. Su, C. H. Chu, G. Sun, *et al.*, "Advances in optical metasurfaces: fabrication and applications," Opt. Express **26**(10), 13148–13182 (2018).
24. S. Choi, J. Zuo, N. Das, *et al.*, "Scalable nanoimprint manufacturing of functional multilayer metasurface devices," Adv. Funct. Mater. **34**(45), 2404852 (2024).
25. J. C. Gutiérrez-Vega, "Pancharatnam–Berry phase of optical systems," Opt. Lett. **36**(7), 1143–1145 (2011).
26. E. Cohen, H. Larocque, F. Bouchard, *et al.*, "Geometric phase from Aharonov–Bohm to Pancharatnam–Berry and beyond," Nat. Rev. Phys. **1**(7), 437–449 (2019).
27. M. Choi, J. Park, J. Shin, *et al.*, "Realization of high-performance optical metasurfaces over a large area: a review from a design perspective," npj Nanophotonics **1**(1), 31 (2024).
28. Y. Wang, Y. Yuan, and K. Zhang, "A review of multi-order diffraction beams: From phase gradient metasurface to metagratings," Adv. Phys. Res. **3**(12), 2400076 (2024).
29. J. Liu, Z. Li, B. Liang, *et al.*, "Remote water-to-air eavesdropping with a phase-engineered impedance matching metasurface," Adv. Mater. **35**(29), 2301799 (2023).

Optics EXPRESS

30. Y. Teng, Y. Xiao, G. Xie, *et al.*, "Multi-channel polarization conversion THz beam splitter based on phase gradient metasurface," Opt. Express **33**(4), 7901–7913 (2025).
31. T. Tian, Y. Liao, X. Feng, *et al.*, "Metasurface-based free-space multi-port beam splitter with arbitrary power ratio," Adv. Opt. Mater. **11**(20), 2300664 (2023).
32. B. Wang, F. Dong, H. Feng, *et al.*, "Rochon-prism-like planar circularly polarized beam splitters based on dielectric metasurfaces," ACS Photonics **5**(5), 1660–1664 (2018).